PCCP

ROYAL SOCIETY OF CHEMISTRY

PAPER

View Article Online
View Journal | View Issue

Check for updates

Cite this: *Phys. Chem. Chem. Phys.*, 2022, **24**, 5529

Regulating the valence level arrangement of high-Al-content AlGaN quantum wells using additional potentials with Mg doping

Shiqiang Lu,[a] Tongchang Zheng,[b] Ke Jiang,[c] Xiaojuan Sun,[c] Dabing Li,[c] Hangyang Chen,[a] Jinchai Li,[a] Yinghui Zhou,[a] Duanjun Cai,[a] Shuping Li,[a] Wei Lin*[a] and Junyong Kang*[a]

Received 20th September 2021,
Accepted 31st January 2022

DOI: 10.1039/d1cp04303j

rsc.li/pccp

Quantum states and arrangement of valence levels determine most of the electronic and optical properties of semiconductors. Since the crystal field split-off hole (CH) band is the top valence band in high-Al-content AlGaN, TM-polarized optical anisotropy has become the limiting factor for efficient deep-ultraviolet (DUV) light emission. Additional potentials, including on-site Coulomb interaction and orbital state coupling induced by magnesium (Mg) doping, are proposed in this work to regulate the valence level arrangement of AlN/$Al_{0.75}Ga_{0.25}N$ quantum wells (QWs). Diverse responses of valence quantum states $|p_i\rangle$ (i = x, y, or z) of AlGaN to additional potentials due to different configurations and interactions of orbitals revealed by first-principles simulations are understood in terms of the linear combination of atomic orbital states. A positive charge and large Mg dopant in QWs introduce an additional Coulomb potential and modulate the orbital coupling distance. For the CH band (p_z orbital), the Mg-induced Coulomb potential compensates the orbital coupling energy. Meanwhile, the heavy/light hole (HH/LH) bands (p_x and p_y orbitals) are elevated by the Mg-induced Coulomb potential. Consequently, HH/LH energy levels are relatively shifted upward and replace the CH level to be the top of the valence band. The inversion of optical anisotropy and enhancement of TE-polarized emission are further confirmed experimentally *via* spectroscopic ellipsometry.

1. Introduction

Quantum confinement is essential for semiconductor device engineering with the rapid development of artificial quantum structures, including quantum wells (QWs), wires, and dots. It has been long established that the relevant quantum states near band edges, that is, the bottom of conduction band (CB) and the top of valence band (VB), determine the critical properties of semiconductors. In the design of QWs, quantum states are commonly understood in terms of the band dispersion and effective mass. However, with structural miniaturization down to the atomistic level, the fundamental physics behind quantum states becomes extremely complex, especially for highly polarized and anisotropic semiconductor systems, such as high-Al-content AlGaN.[1]

Generally, the top of valence bands in high-Al-content AlGaN can be separated into heavy (HH), light (LH), and crystal field split-off (CH) hole bands. In view of more complicated quantum states at the top of the valence band as compared to that at the bottom of the CB, arrangement of valence bands governs not only hole carriers, but also optical transition probability and anisotropy of semiconductors. It has been reported in previous studies that the p_z orbital, which presents a strong head-over-head lobe structure along the [0001] direction, mainly contributes to the CH band in AlGaN multiple QWs (MQWs) with the Γ_7 symmetry. Radiative emission related to the CH band exhibits an abnormal behavior insensitive to external electric fields. By comparison, HH (Γ_9) and LH (Γ_7) bands are mainly contributed by p_x and p_y orbitals, which present a side-by-side in-plane lobe structure, and radiative emission from HH/LH bands is dependent on external electric fields.[2] The diverse orbital configurations and orientations for CH and HH/LH bands also give rise to different additional orbital inter-coupling energies. The ppσ coupling between p_z orbitals compensates, while, the ppπ coupling between p_x/p_y orbitals enhances the band offset of AlGaN MQWs, accounting for the abnormal confinement behavior of the $|p_z\rangle$ state, in

[a] Fujian Key Laboratory of Semiconductor Materials and Applications, CI Center for OSED, Department of Physics, Xiamen University, Xiamen 361005, China. E-mail: linwei@xmu.edu.cn, jykang@xmu.edu.cn
[b] Department of Physics, School of Science, Jimei University, Xiamen 361021, China
[c] State Key Laboratory of Luminescence and Applications, Changchun Institute of Optics, Fine Mechanics and Physics, Chinese Academy of Sciences, Dongnanhu Road No. 3888, Changchun 130033, China

contrast to localized $|p_x\rangle$ and $|p_y\rangle$ states.[3] In addition, the different constituent orbitals at the valence band edge hint at the fact that the interaction between p_z or p_x/p_y orbitals tends to invoke a long range Coulomb effect varying from states to states. In light of the orbital state coupling, the quantum confinement at the atomic scale requires consideration of various additional potentials, such as Coulomb interaction and orbital inter-coupling, depending on the given orientations, configurations, and interactions of orbitals. The distinct orbital characters and behaviors can also be utilized to regulate valence quantum states of AlGaN subtly, and produce the desired electronic and optical properties to enhance the performance of AlGaN optoelectronic devices.

In low-Al-content $Al_xGa_{1-x}N$ ($x < 0.4$), the top valence band is the HH/LH bands, thus the optical transition occurs mainly between the CB and HH/LH bands, resulting in a dominant TE polarized emission. However, a common feature observed in high-Al-content AlGaN MQWs is that the CH band composed of the p_z orbital tends to be the top valence quantum level. The related optical transition between conduction and CH bands at the band edge exhibits TM polarization.[4,5] Unlike HH/LH-related TE-polarized light emission, the TM polarized light propagates laterally in the well plane limiting light extraction in AlGaN for deep-ultraviolet (DUV) light-emitting diodes (LEDs).[6–8] Besides, the p_z orbital inter-coupling is likely to be delocalized for holes[3] accompanied by the quantum confined Stark effect (QCSE),[9,10] which considerably reduces the radiative emission in DUV LEDs. The fundamental mechanism governing the optical anisotropy and quantum confinement is rooted in constituent orbitals for quantum states in AlGaN. Therefore, regulating valence quantum states of high-Al-content AlGaN MQWs to change the valence level arrangement and enhance the carrier confinement becomes crucial for future design of high performance active regions of DUV LEDs.[11–13]

In this work, magnesium (Mg) doping as an effective method is proposed to introduce an additional Coulomb potential and modulate the orbital state coupling for $AlN/Al_{0.75}Ga_{0.25}N$ QWs. By regulating these two additional potentials, Mg doping successfully inverts the valence level arrangement and enhances the TE-polarized emission. First-principles simulations were conducted to analyze the configuration and spatial distribution of valence quantum states $|p_i\rangle$ ($i = x, y$, or z) in CH and HH/LH bands of undoped and Mg-doped $AlN/Al_{0.75}Ga_{0.25}N$ QWs. Additional potentials introduced by orbital state coupling, polarization field, and Coulomb interaction with the aid of the linear combination of atomic orbitals (LCAO) approach were calculated to investigate the quantum confinement mechanism of QWs. Experimentally, undoped and Mg-doped $AlN/Al_{0.75}Ga_{0.25}N$ MQWs were epitaxially grown. Raman spectra were recorded to investigate the local lattice variation. The inversion of optical anisotropy and enhancement of TE-polarized emission were further confirmed using spectroscopic ellipsometry.

2. Experimental section

Theoretically, first-principles simulations were carried out using the Vienna ab initio simulation package (VASP) in the framework of density functional theory (DFT).[14,15] The Perdew–Burke–Ernzerhof (PBE) generalized gradient approximation (GGA) method was utilized for exchange–correlation interactions among electrons.[16] It is well known that the conventional GGA calculation commonly underestimates the band gap of semiconductors and hybrid DFT can correct these issues. Although more refined approaches are reported in the literature, the GGA has been shown to be able to provide, at least qualitatively, a correct description of the intraband structure in the cases of III–V quantum structures with no adjustable parameters, which allows for establishing general trends in the valence band structure in the present study.[17–20] QW models were generated using $2a \times 2a \times 14c$ primitive cells constructed with 9 monolayers of the $Al_{0.75}Ga_{0.25}N$ well and 19 monolayers of the AlN barrier. The choice of barrier width is thick enough to prevent the inter-well interaction effect. An Mg atom was doped at the center of the well on the basis of the undoped QW model to regulate the orbital state coupling and Coulomb potentials. Ga 3d electrons were treated as part of valence electrons. The $8 \times 8 \times 3$ Monkhorst–Pack grid of k points was used for sampling the Brillouin zone. A cutoff energy of 520 eV was used to expand the electronic wavefunctions, which was sufficient for the plane wave basis to achieve energy convergence. Geometry optimizations were performed by relaxing all degrees of freedom using conjugate gradient algorithm with convergence energies of 1×10^{-3} and 1×10^{-4} eV for ions and electrons, respectively.

First-principles simulations were used to accurately calculate the electronic properties of QWs which were further explained in terms of a tight-binding based LCAO approach. Optimized QW structures (*i.e.* the bond distances) calculated by DFT were used as input to extract the orbital state coupling energy.[3,21] Combining first-principles and LCAO, the fundamental physics between the additional potentials and valence arrangement was investigated. DOS was projected onto p_x, p_y, and p_z orbitals for valence bands in the k-space to identify constituent states. Orbital-dependent wave function characteristics were projected onto each atom in local coordinates (xyz) with the z-axis parallel to the c-axis of the crystal and the x-axis parallel to the [10−10] crystalline direction. The self-consistent local potential distribution along the [0001] direction was calculated using the macroscopic average technique, and the minimum potential point was set to 0 eV as the reference to illustrate the band offset and polarization-induced band tilting of QWs.[22] Layer-decomposed DOS was illustrated along the [0001] direction, with the DOS value represented by a continuous color variation from blue to red, to visualize band profiles of QWs in real space.[23]

Experimentally, epitaxial growth was conducted on a c-plane sapphire substrate *via* metal organic vapor phase epitaxy (MOVPE). Source precursors of Al, Ga, and N were trimethylaluminum (TMA), trimethylgallium (TMG), and ammonia (NH_3), respectively. Bis-cyclopentadienyl magnesium (Cp_2Mg) and hydrogen (H_2) were used as the Mg impurity source and carrier gas, respectively. MQW samples were grown on an AlN buffer layer, followed by a 1.3 μm AlN layer, and finally 20 periods of

AlN/$Al_{0.75}Ga_{0.25}N$ MQWs. The thickness of the barrier and well was set to 10 and 3 nm, respectively. Undoped and Mg-doped MQWs were grown by introducing 0, 80, and 160 sccm of Cp_2Mg gas flow into the reactor during the growth of central well layers. The corresponding Mg doping concentrations are approximately 0, 2.0×10^{18}, and 5.0×10^{18} cm^{-3}, and samples are denoted MQWs A, B, and C, respectively. Raman measurement was conducted using a Raman microscope (WITec alpha 300RA) with a 488 nm laser. High-resolution transmission electron microscopy (HRTEM) was performed to characterize the structural and crystalline qualities of MQWs (Talos F200). Spectroscopic ellipsometry (Jobin Yvon UVSEL FUV200) was used to measure dielectric function spectra due to its sensitivity to complex optical responses. Measurements were performed in the energy range of 1.5 to 6.5 eV, with an increase of 0.01 eV, at an incident angle of 70°. The ellipsometer operated with a phase-modulated polarizer and an analyzer, and a xenon lamp was used as the light source. The dispersion model of Tanguy was used to avoid any possibility of artificial data and minimize error during extraction of the dielectric function.[24,25] All major contributions from the complete structure of samples, including semi-infinite *c*-plane uniaxial sapphire substrate, AlN buffer layer, AlN thick layer, anisotropic AlN/$Al_{0.75}Ga_{0.25}N$ MQWs (ordinary and extraordinary refraction indexes as fitting parameters), and thin overlayers, were considered.[26] Fitting errors of all samples are smaller than 0.8, thereby indicating excellent reliability and accuracy of simulations.

3. Results and discussion

Quantum confinement mechanism

The quantum confinement behavior of a carrier is inherently linked to the band profile of QWs in the real space. In the design of QW band engineering, the band profile based on the band offset between the $Al_xGa_{1-x}N$ well and the $Al_yGa_{1-y}N$ barrier ($y > x > 0.5$) initiated with a symmetrical square potential well model, which serves as a good starting point for understanding the electronic structure for AlGaN QWs. Taking into account the spontaneous and piezoelectric polarization, the tilted triangular potential well model is widely adopted to explain the complex quantum behavior in highly polarized AlGaN QWs, such as the well-known QCSE. However, the band profile of the triangular well model is treated with simply linear tilting in many cases,[23] which is inadequate to describe all details of AlGaN QWs. In particular, when the quantum structure is down to the atomic scale, discontinuities at the interfaces originating from the formation of the atomic orbital coupling on the quantum confinement become significant.[3] The practical band profile are largely concerned with band offset, additional potentials induced by polarization field and orbital state inter-coupling, which are crucial for understanding the complex quantum confinement mechanism in high-Al-content AlGaN QW.

To shed light on the quantum confinement at the top of the valence band in undoped $Al_{0.75}Ga_{0.25}N$/AlN QWs, the electronic structure near the valence band maximum (VBM) was calculated and analyzed *via* first-principles simulations, as shown in Fig. 1 and 2. The undoped QWs are illustrated in Fig. 1a and Fig. 2a, accompanied by isosurface plots of the orbital-projected partial charge density for p_z and p_x orbitals (p_y orbital is similar to p_x) in Fig. 1b and 2b, respectively. The partial charge density is extracted from the CH (p_z orbital) or HH/LH (p_x/p_y) quantum levels along the Γ–A path of k-space. In the AlGaN QWs constructed along the c direction, *i.e.*, the [0001] direction of nitride, the top of the valence bands along the Γ–A path exhibits flat and discrete quantum levels due to the strong confinement effect (as shown in Fig. 5a and b), which determine most properties of optical transitions. For the p_z orbital, charges are located around the interface region between the left barrier and center well, and extend to the barrier region by approximately 10 monolayers, demonstrating the delocalized behavior.[3] By close inspection of the orbital configuration, it can be found that $|p_z\rangle$ states show a two-lobed-shape charge distribution parallel to the z direction, which can overlap with each other in a head-over-head fashion along the [0001] direction (right inset in Fig. 1c). While, for the p_x orbital (Fig. 2b), most of charges are located in the well region close to the left interface. Compared with the p_z orbital, the corresponding charge distribution of $|p_x\rangle$ states is more localized in the well region and only extends into the barrier region by approximately two monolayers, demonstrating the localization feature. In addition, $|p_x\rangle$ states exhibit (0001) in-plane lobe configuration and overlap with each other in a side-by-side fashion along the z direction (right inset in Fig. 2c).

It has been pointed out in previous studies[3] that inter-coupling between p states typically contains ppσ coupling and ppπ coupling according to the tight-binding based LCAO method. For p states oriented other than purely σ or π, the state can be decomposed into a σ-oriented component and a π-oriented component by symmetry. To extract the additional coupling energy ΔV in the QW potential along the quantum confinement direction in line with the z direction, one can decompose the interactions into the ppσ and ppπ coupling as follows:[21]

$$\begin{aligned}\Delta V &= \frac{3}{4}\left(V_{pp\sigma}\cos^2\delta + V_{pp\pi}\sin^2\delta\right)\\ &= \frac{3\hbar^2}{4md^2}\left(2.22\cos^2\delta - 0.63\sin^2\delta\right),\end{aligned} \tag{1}$$

where d is the distance between the nearest p_i orbital, and δ is the misaligned angle between the p_i orbitals.[3,21,27,28] Fig. 1c and 2c display the variation in the coupling distance between nearest N atoms across the well and barrier. Lattice discontinuity between the barrier and well region can be clearly observed, which originates from the difference in the Al-content between the two areas. Based on the calculated d, the additional orbital coupling energy of p_z orbitals ΔV derived from eqn (1) is illustrated in Fig. 1d. The average local potential value along the [0001] direction was also calculated to illustrate the band offset and polarization-induced band titling of QWs, as shown in Fig. 1e. As illustrated in Fig. 1f, the layer-decomposed DOS of the $|p_z\rangle$ state was induced to visualize the band profile in the real space of undoped QWs.

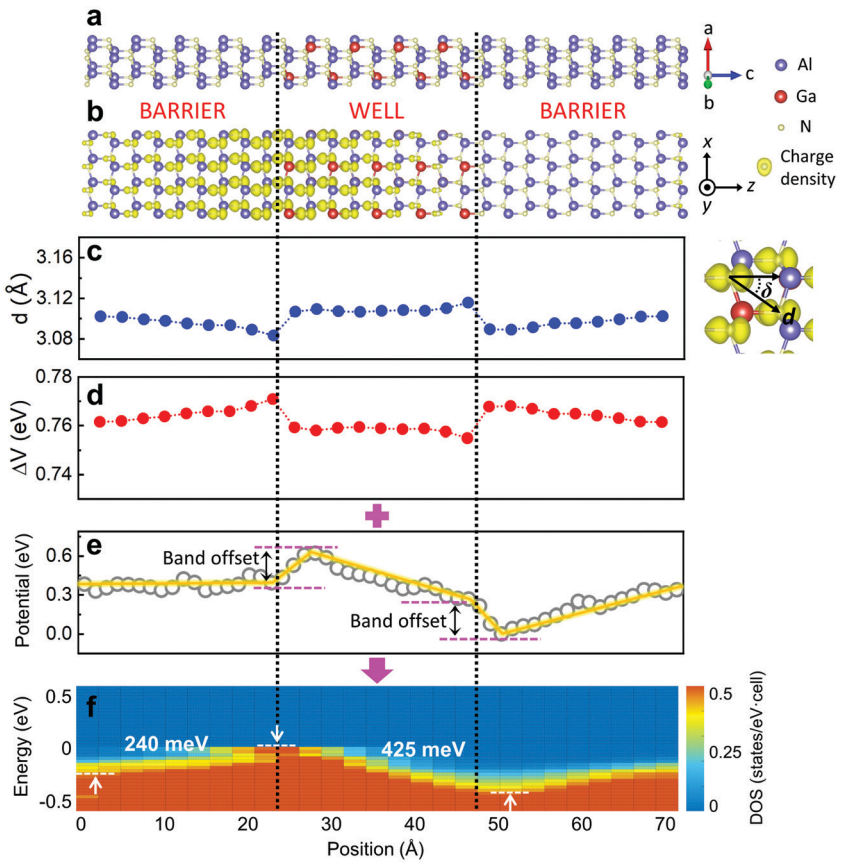

Fig. 1 Electronic structures around the VBM for undoped QWs contributed by the p_z orbital (z is perpendicular to the plane of the QWs). (a) Crystal structure of undoped $Al_{0.75}Ga_{0.25}N/AlN$ QWs. (b) Surfaces corresponding to a charge density of 3×10^{-5} e Å^{-3} for the p_z orbital extracted from the CH quantum level along the Γ–A path of k-space. The z-axis is along the [0001] direction of the wurtzite lattice. (c) Distance d variation between nearest N atoms. (d) Coupling potential between p_z orbitals. The p_z orbital intercoupling can be decomposed into ppσ- and ppπ-oriented components. (e) Schematic of the band offset and polarization induced band tilting based on the calculated average potential value. (f) Layer- and p_z orbital-projected DOS at the VBM.

A larger atomic separation d in the well causes a decrease in the p_z orbital coupling energy compared with that in the barrier, as shown in Fig. 1d. This variation and discontinuity of the p_z coupling energy between the barrier and well compensate the quantum barrier height induced by the band offset. In addition, the polarization field further provides an additional potential with tilted and asymmetric shape to the band profile along the z direction, which is the typical characteristic of QCSE (Fig. 1e). Accordingly, as shown in Fig. 1f, the band profile of the undoped QWs has a tilted and rather flat configuration at the maximum valence energy level, that is, the p_z orbital-contributed CH band. This leads to a very small quantum barrier height for the QWs (around 240 and 425 meV for left and right sides, respectively). This tilted band profile drives holes of $|p_z\rangle$ states to the left interface of the barrier and well, and small potential barriers that provide only minimal confinement for hole carriers cause the delocalized distribution of $|p_z\rangle$ holes into the barrier (Fig. 1b).

A similar analysis can be conducted for the band profile constructed by p_x or p_y orbitals. As indicated in Fig. 2b and the right inset of Fig. 2c, the $|p_x\rangle$ or $|p_y\rangle$ state in HH/LH bands induced orbital inter-couplings can also be decomposed into two components according to eqn (1). The additional orbital coupling energy ΔV of p_x orbitals, derived from eqn (1) was calculated and is illustrated in Fig. 2d. The larger atomic separation d in the well also decreases the coupling energy ΔV in the well compared with that in the barrier. However, the decreased value from the barrier to well is much smaller than that in the case of p_z orbitals. Consequently, combining with the polarization-induced additional potential and the band offset shown in Fig. 2e, the quantum barrier heights of the $|p_x\rangle$ or $|p_y\rangle$ states are much higher compared with those of the p_z orbitals. As illustrated by the layer-decomposed DOS in Fig. 2f, the band profile of the $|p_x\rangle$ or $|p_y\rangle$ state is tilted, but with a less flat character compared with that of the p_z orbital. Quantum barriers for $|p_x\rangle$ or $|p_y\rangle$ hole carriers are 350 and 550 meV in the left and right sides of QWs, which are 110 and 125 meV higher than those of the p_z orbital, respectively. The stronger quantum confinement for $|p_x\rangle$ or $|p_y\rangle$ hole states attributed by increased barriers is consistent with the localized behavior, as shown in Fig. 2b. These results indicate that the quantum confinement of QWs is greatly dependent on

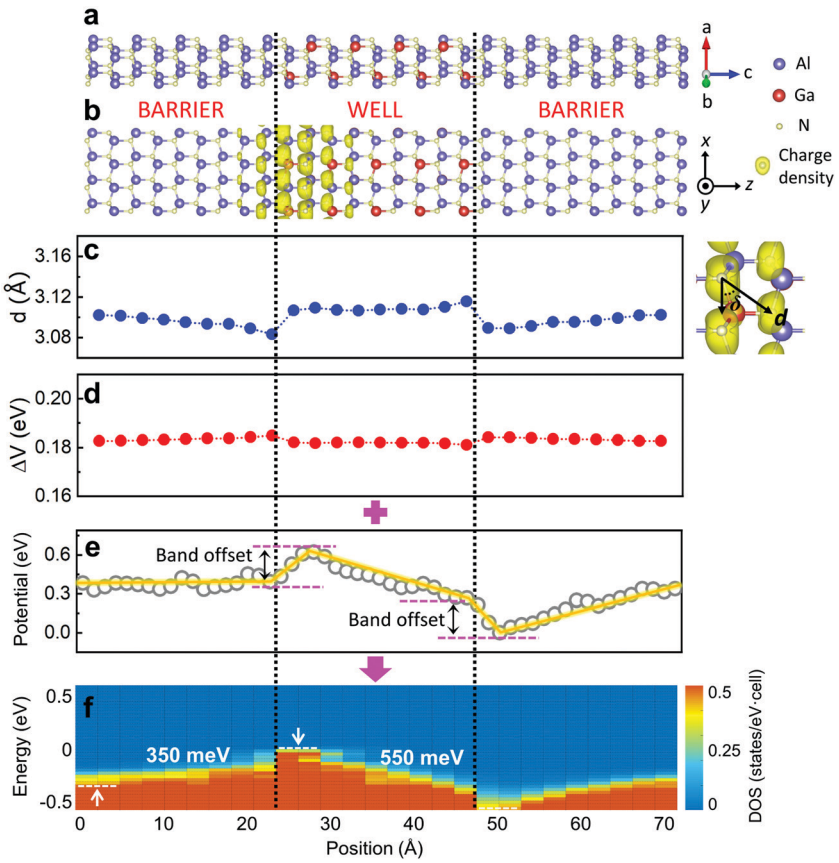

Fig. 2 Electronic structures around the VBM for undoped QWs contributed by the p_x orbital (x is parallel to the plane of the QWs). (a) Crystal structure of undoped $Al_{0.75}Ga_{0.25}N$/AlN QWs. (b) Surfaces corresponding to a charge density of 3×10^{-5} e Å^{-3} for the p_x orbital extracted from the HH/LH quantum levels along the Γ–A path of k-space. The z-axis is along the [0001] direction of the wurtzite lattice. (c) Distance d variation between nearest N atoms. (d) Coupling potential between p_x orbitals. The p_x orbital intercoupling can be decomposed into ppσ- and ppπ-oriented components. (e) Schematic of the band offset and polarization induced band tilting based on the calculated average potential value. (f) Layer- and p_x orbital-projected DOS at the VBM.

additional potentials, such as polarization field and orbital state inter-coupling, closely linking to the orientations, configurations, and interactions of orbitals.

Regulation of valence quantum states using additional potentials with Mg doping

Based on the abovementioned results, it becomes clear that the weakened quantum confinement and reduction of carrier overlap are highly dependent on the various additional potentials in the valence band, which can be utilized to overcome the obstacles under consideration by modulating valence quantum states in high-Al-content AlGaN QWs. According to eqn (1), the orbital inter-coupling energy is closely related to the coupling distance. Impurity doping turns out to be advantageous for regulating the coupling energy by introducing local lattice variation as well as additional Coulomb potential to QWs due to the Coulomb interaction between carriers and the charged dopant atoms. The Mg atom commonly serves as the acceptor for p-type doping in group-III nitrides,[29–31] and previous studies have reported that using Mg doping in InGaN MQWs can improve the hole injection and crystal quality, thus enhancing the performance of InGaN LEDs.[32,33] When Mg is doped in nitride *via* the substitution of Ga or Al, a local positive center is formed due to the lack of a single valence electron. The interaction between hole carriers and Mg will introduce an additional Coulomb potential to QWs. Moreover, given the larger radius of the Mg atom (145 pm) than those of Ga (136 pm) and Al (118 pm),[34,35] Mg doping will produce additional distortion to the local lattice, and lead to the variation of coupling distance between orbitals, which can be utilized to regulate the orbital coupling energy. Based on these analyses, Mg doping in the QWs is designed for regulating quantum states in the valence band of high-Al-content AlGaN QWs *via* additional potential engineering.

As shown in Fig. 3a and 4a, the Mg atom was doped at the center of the well by substituting Ga on the basis of the undoped QW model. Fig. 3b shows the p_z orbital-projected partial charge density for Mg-doped QWs. It is observed that charges have been shifted integrally into the center of well compared with the undoped QWs. The effective confinement of $|p_z\rangle$ hole states in the Mg-doped well is beneficial for electron–hole overlap and radiative emission. Fig. 3c depicts the variation in the distance for p_z orbitals between nearest N atoms. The d in the plane closed to Mg increases with Mg being doped

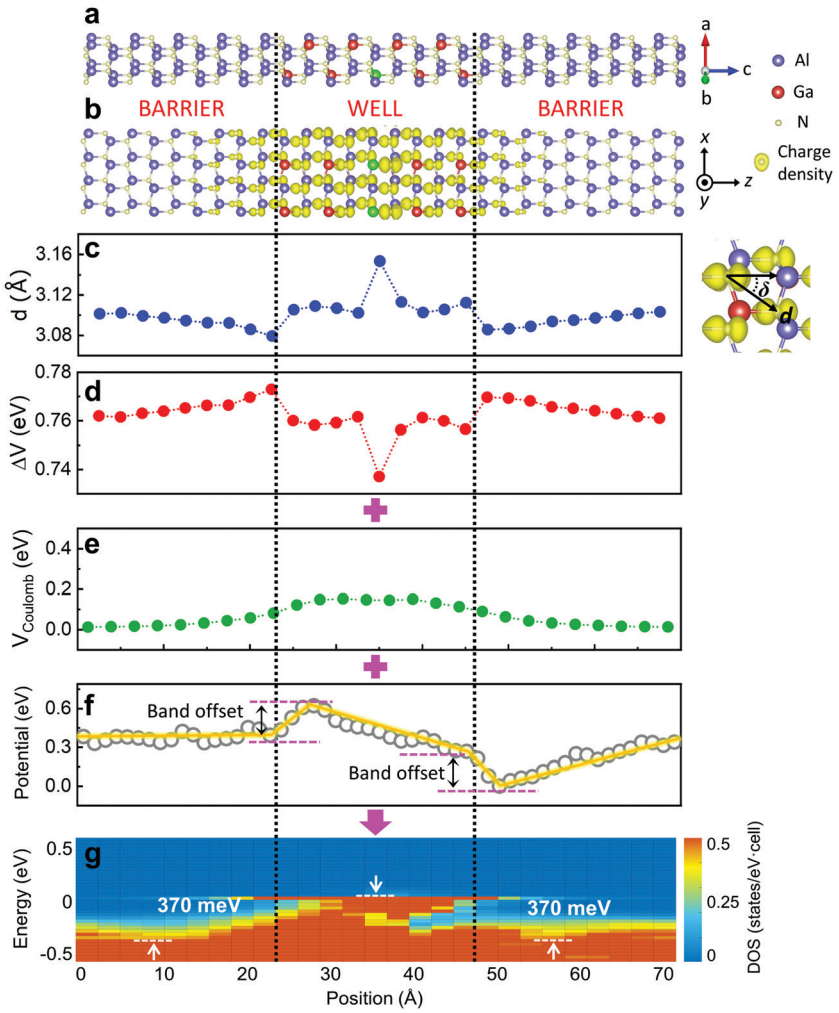

Fig. 3 Electronic structures around the VBM for Mg-doped QWs contributed by the p_z orbital (z is perpendicular to the plane of the QWs). (a) Crystal structure of Mg-doped $Al_{0.75}Ga_{0.25}N$/AlN QWs. (b) Surfaces corresponding to a charge density of 3×10^{-5} e Å^{-3} for the p_z orbital extracted from the CH quantum level along the Γ–A path of k-space. The z-axis is along the [0001] direction of the wurtzite lattice. (c) Distance d variation between nearest N atoms. (d) Coupling potential between p_z orbitals. The p_z orbital intercoupling can be decomposed into ppσ- and ppπ-oriented components. (e) Mg-Induced Coulomb potential for the charge of the p_z orbital. (f) Schematic of the band offset and polarization induced band tilting based on the calculated average potential value. (g) Layer- and p_z orbital-projected DOS around the VBM.

at the well due to the large radius of Mg. Consequently, as illustrated in Fig. 3d, the additional coupling energy ΔV of p_z orbitals reduces by approximately 24.5 meV around the plane with Mg doping.

Meanwhile, Mg is a local positive center that also introduces an additional Coulomb potential to the band profile of QWs due to the interaction with hole carriers. According to the basic electromagnetic theory, the Coulomb potential induced by the interaction between hole carriers and Mg can be simply calculated as follows:

$$V_{\text{Coulomb}} = e\int_0^{L/2} \frac{1}{4\pi\varepsilon_0}\frac{Q(z)}{L/2 - z}\mathrm{d}z + e\int_{L/2}^{L} \frac{1}{4\pi\varepsilon_0}\frac{Q(z)}{z - L/2}\mathrm{d}z, \quad (2)$$

where L is the thickness of QWs, ε_0 is the permittivity of vacuum, $Q(z)$ is the charge density, z is the position along the [0001] direction. The Mg-induced Coulomb potential for the charge of p_z orbital based on eqn (2) is illustrated in Fig. 3e. Compared with the localized interaction of orbital intercoupling, the long range Coulomb interaction is capable of extending into the entire area of the barrier and well. The Coulomb potential for the p_z orbital is also relatively flat and smooth across the entire QW due to the delocalized distribution of $|p_z\rangle$ quantum states. Moreover, the Coulomb potential induced by Mg in the well region is larger than that in the barrier region. This increased Coulomb potential in the well region compensates the reduced orbital coupling energy induced by Mg. Therefore, the height of the quantum barrier in two interfaces for the p_z orbital of Mg-doped QWs is similar to that in the case of undoped QWs (Fig. 3g). In spite of this, the additional Coulomb potential at the center of the well region is much larger than that at the interfaces of the well and barrier. Hence the band tilting induced by the intrinsic polarization potential is significantly reduced, which infers the suppression

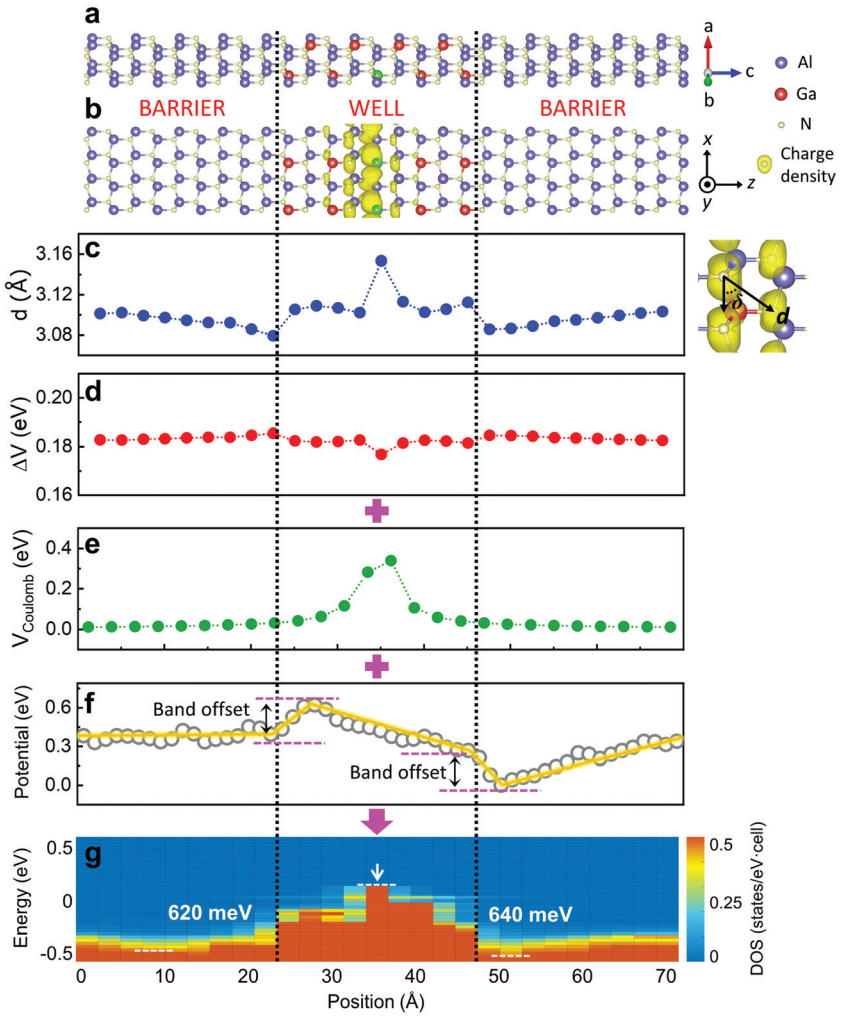

Fig. 4 Electronic structures around the VBM for Mg-doped QWs contributed by the p_x orbital (x is parallel to the plane of the QWs). (a) Crystal structure of Mg-doped $Al_{0.75}Ga_{0.25}N$/AlN QWs. (b) Surfaces corresponding to a charge density of 3×10^{-5} e Å^{-3} for the p_x orbital extracted from the HH/LH quantum levels along the Γ–A path of k-space. The z-axis is along the [0001] direction of the wurtzite lattice. (c) Distance d variation between nearest N atoms. (d) Coupling potential between p_x orbitals. The p_x orbital intercoupling can be decomposed into ppσ- and ppπ-oriented components. (e) Mg-Induced Coulomb potential for the charge of the p_x orbital. (f) Schematic of the band offset and polarization induced band tilting based on the calculated average potential value. (g) Layer- and p_x orbital-projected DOS around the VBM.

of QCSE. The confinement is consequently enhanced, as confirmed by the layer- and p_z orbital-projected DOS diagram and partial charge density distribution shown in Fig. 3g and b, respectively. Therefore, the majority of $|p_z\rangle$ quantum states are redistributed at the center of QWs.

Additional potential engineering *via* Mg doping modulates the band profile and enhances the hole confinement more significantly for p_x and p_y orbitals. Fig. 4b shows the p_x orbital-projected partial charge density for the Mg-doped QWs. Compared with the case of undoped QWs, the distribution of localized $|p_x\rangle$ hole states in the Mg-doped QWs shifts to the center of the well, and further experiences a significant volume shrinkage. Strongly confined $|p_x\rangle$ hole states at the center of QWs will increase the electron–hole overlap and radiative emission rate. According to the increased d induced by Mg doping (Fig. 4c), the additional coupling energy ΔV of p_x orbitals slightly decreases by approximately 5.8 meV in the plane with Mg doping, as shown in Fig. 4d. Moreover, the Mg-Induced Coulomb potential for the charge of the p_x orbital based on eqn (2) is calculated and illustrated in Fig. 4e. The Mg-induced Coulomb potential for the p_x orbital is significantly larger and more concentrated at the center of QWs compared with that in the case of the p_z orbital. This phenomenon contributes to the side-by-side in-plane lobe structure of the p_x orbital and the strongly localized behavior of $|p_x\rangle$ quantum states. Compared with delocalized p_z orbital states, which present a head-over-head lobe structure along the confinement direction, the Coulomb interaction between p_x orbital states and Mg is significantly larger and more concentrated around the center of the quantum well. Consequently, combining with the orbital coupling energy, the energy levels of $|p_x\rangle$ quantum states in the QWs are significantly increased, and the height of quantum barriers in the left and right interfaces of QWs is also greatly increased. This finding can be confirmed in the

layer- and p_x orbital-projected DOS diagram shown in Fig. 4g. Band tilting and bending are also evidently compensated and suppressed by Mg-induced additional potentials. Quantum barriers for $|p_x\rangle$ hole carriers are 620 and 640 meV in the left and right sides of Mg-doped QWs. These values are 270 and 90 meV higher than those for the p_x orbital in the undoped QWs, and are 250 and 270 meV higher than those for the p_z orbital in Mg-doped QWs, respectively. Suppressed band tilting and increased quantum barriers provide a significantly stronger quantum confinement for the $|p_x\rangle$ states, and lead to strongly localized and concentrated charge distribution at the center of Mg-doped QWs (Fig. 4b).

These additional potentials induced by Mg doping not only compensate or enhance quantum barriers for the band profile in the real space, but also directly affect energy levels and relative arrangement of valence bands (CH, HH, and LH) in the *k*-space of $AlN/Al_{0.75}Ga_{0.25}N$ QWs. Fig. 5a and b show the electronic band structures of undoped and Mg-doped QWs in the *k*-space from Γ to *A* point, respectively. The energy of p_x and p_y orbital-contributed quantum levels is increased by Mg doping, with respect to that of p_z orbital-contributed quantum levels. The physical mechanism behind this valence level rearrangement is rooted in the increased energy levels of $|p_x\rangle$ quantum states due to enhanced additional potential terms, including orbital coupling and Coulomb interaction with Mg. Generally, the optical anisotropy of AlGaN is characterized by the crystal-field splitting energy Δ_{cr} representing the energy difference between HH/LH and CH bands. Increasing the Δ_{cr} value in Al-rich AlGaN is favorable to improve the TE-polarized light emission and light extraction efficiency of DUV LEDs. As shown in Fig. 5a, the Δ_{cr} of undoped QWs is −24.0 meV, indicating the dominant emission light with TM polarization. For Mg-doped QWs (Fig. 5b), the Δ_{cr} is increased to positive 122.3 meV, suggesting that the emission light at the band edge is reversed to be the TE polarization *via* Mg doping.

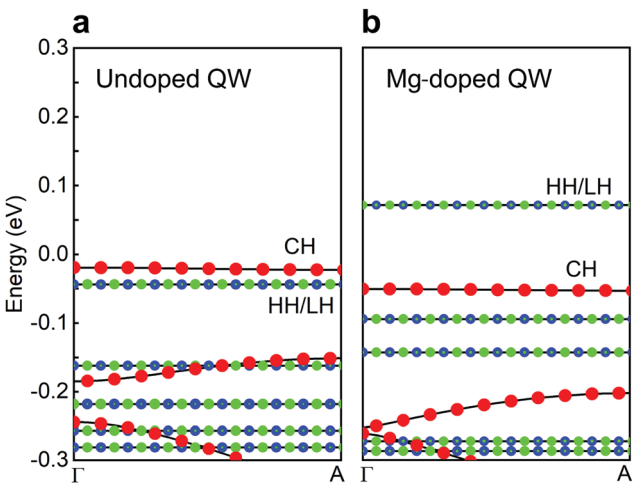

Fig. 5 Electronic band structures around the VBM. (a) Undoped $Al_{0.75}Ga_{0.25}N/AlN$ QWs and (b) Mg-doped $Al_{0.75}Ga_{0.25}N/AlN$ QWs. The p_x, p_y, and p_z contributions to the eigenstates at each *k*-point are indicated by the size of blue, green, and red circles, respectively.

The spontaneous emission rate R_{sp} of QWs can be calculated using Fermi's golden rule as follows:[36]

$$R_{sp} = C \times \int h\nu_{CV} \left|\overline{M_T}(E_{CV})\right|^2 \rho_r(E_{CV}) f_V (1 - f_C) \mathrm{d}E_{CV}, \quad (3)$$

where C is a constant, E_{CV} is the transition energy from the conduction band to the valence band, h is the Planck constant, ν_{CV} is the frequency of the generated light, ρ_r is the reduced density of states, f_C and f_V are the Fermi–Dirac distribution for electrons and holes, and $\overline{M_T}(E_{CV})$ is the transition matrix element. As compared to that for the TE-polarized light emission in the undoped QWs, the R_{sp} of TE-polarized light emission significantly increases by approximately 13.38 times after Mg doping. The increased spontaneous rate strongly confirms the enhanced TE-polarized emission because of the additional potential modulation *via* Mg doping.

Experimentally enhancing TE-polarized emission of MQWs *via* Mg doping

Furthermore, the concept of additional potential modulation *via* Mg doping is demonstrated experimentally by designing and growing undoped $AlN/Al_{0.75}Ga_{0.25}N$ MQWs A, slightly Mg-doped MQWs B, and heavily Mg-doped MQWs C *via* MOVPE. The complete epitaxial structure of MQWs sample is shown in Fig. 6a and c, including an AlN buffer layer, a 1.3 μm AlN layer, and 20 periods of $AlN/Al_{0.75}Ga_{0.25}N$ MQWs. Fig. 6b presents the cross-sectional HRTEM image of the Mg-doped $AlN/Al_{0.75}Ga_{0.25}N$ MQWs (MQWs B). The flat and sharp interfaces of MQWs are clearly recognized, which suggests the good structural and crystalline quality of MQWs. The growth of barriers and wells agrees well with the structure design. Based on the TEM results, the high quality of the as-grown $AlN/Al_{0.75}Ga_{0.25}N$ MQWs can be confirmed and the experimental structure is closed to the simulation model.

Mg doping-induced variation of *d* can be detected from the strain conditions of MQWs taking into account that the distance variation between nearest N atoms is represented in the lattice distortion. It is generally believed that *d* along the *z* direction gradually lengthens when the strain conditions of the lattice transfers from tensile to compressive, as shown in the inset of Fig. 6d. To characterize strain conditions of the well region of MQWs, Raman measurement was conducted on samples. As shown in Fig. 6d, the typical E_2(high) GaN-like mode allowed by the Raman selection rule is observable in the Raman spectra.[37] The shift of the E_2(high) GaN-like mode is sensitive to the biaxial strain conditions of AlGaN.[38] It is noted that Ga only exists in the quantum well region in the present case of $AlN/Al_{0.75}Ga_{0.25}N$ MQWs, so that, the GaN-like mode can accurately reflect the strain conditions of the $Al_{0.75}Ga_{0.25}N$ well without the signal influence from the AlN barrier region. The E_2(high) GaN-like mode under zero stress with 75% Al composition is located at 610.8 cm^{-1}, as indicated by the dotted line in Fig. 6d.[39] The peaks of the E_2(high) GaN-like mode for undoped MQWs A, slightly Mg-doped MQWs B and heavily Mg-doped MQWs C are located at 614.8 cm^{-1}, 618.2 cm^{-2}, and 621.3 cm^{-1}, respectively, suggesting that Mg doping enhances the compressive strain in the $Al_{0.75}Ga_{0.25}N$ well. More

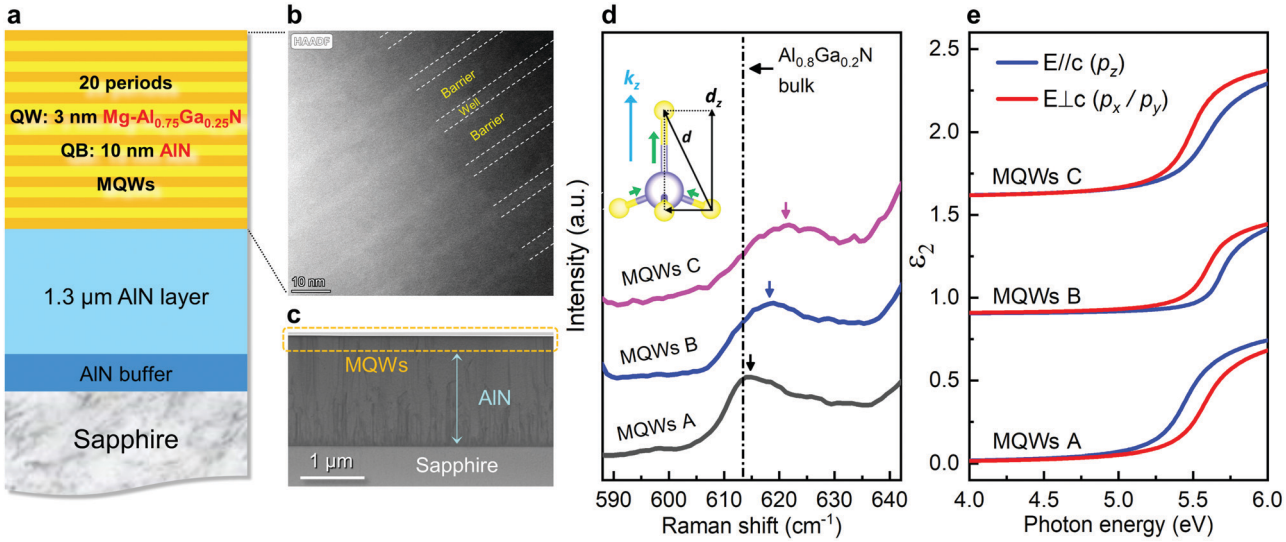

Fig. 6 Characterizations of Mg-doped MQWs. (a) Schematic of the high-Al-content $Al_{0.75}Ga_{0.25}N$/AlN MQWs. (b) Cross-sectional HRTEM image of the Mg-doped MQWs B. (c) Cross-sectional TEM image of the complete epitaxial structure. (d) Raman spectra of the E_2(high) GaN-like mode for undoped MQWs A and Mg-doped MQWs B and C. The dash line indicates the stress-free position. The inset shows the lattice distortion under compressive strain. (e) Spectroscopic ellipsometry spectra on two perpendicularly polarized directions.

importantly, this strain variation confirms the enlarged orbital coupling distance between two nearest N atoms by Mg doping, which is consistent with simulation results.

Spectroscopic ellipsometry was further applied to verify the valence level regulation using additional potentials with Mg doping and measure dielectric function spectra of MQWs, as shown in Fig. 6e. A close inspection of the onset of ε_2 of MQWs A shows that band-edge lines of $\varepsilon_2^{\parallel}$ and $\varepsilon_2^{\perp}$ are clearly separated from each other, and the threshold energy of $\varepsilon_2^{\parallel}$ is lower than that of $\varepsilon_2^{\perp}$. This finding implies that the optical properties of undoped AlN/$Al_{0.75}Ga_{0.25}N$ MQWs are highly anisotropic and TM-polarized emission will be dominant. Hence, the p_z orbital-contributed CH band is the top valence band in undoped MQWs. Noticeably, onset positions of $\varepsilon_2^{\parallel}$ and $\varepsilon_2^{\perp}$ have been switched over, and the threshold energy of $\varepsilon_2^{\perp}$ becomes lower than that of $\varepsilon_2^{\parallel}$ for Mg-doped MQWs B and C. Compared with the slightly doped MQWs B, the intensity of $\varepsilon_2^{\perp}$ is further enhanced for heavily Mg-doped MQWs C. The increased contribution of $\varepsilon_2^{\perp}$ at the band edge strongly confirms that the HH and LH bands have replaced the CH band to be the top valence bands, and the TE-polarized emission will be enhanced in Mg-doped AlN/$Al_{0.75}Ga_{0.25}N$ MQWs. Consequently, the concept of additional potential modulation is verified through impurity doping to regulate valence quantum states of high-Al-content AlGaN MQWs, which are expected to be applicable to other semiconductor systems, especially for materials with strong polarization and anisotropy, such as InGaN and ZnMgO.

4. Conclusions

In conclusion, the regulation of the valence level arrangement of AlN/$Al_{0.75}Ga_{0.25}N$ QWs is demonstrated by modulating additional potentials, including on-site Coulomb interaction and orbital state coupling induced *via* Mg doping. Based on first-principles simulations, the quantum confinement in QWs is understood in terms of the additional potentials with the LCAO introduced by orbital state inter-coupling, polarization field, and Coulomb interaction. Mg doping in the quantum well was performed to regulate orbital coupling and Coulomb interaction. By greatly increasing the Coulomb potential with Mg doping, the height of quantum barriers is greatly increased for the p_x and p_y orbitals, which suggests the enhanced hole confinement. In addition, the HH/LH bands are relatively lifted up to be the top valence band by the additional potential terms with Mg doping, leading to an enhanced TE-polarized emission. Experimentally, the valence level rearrangement and dominant TE emission were successfully achieved in Mg-doped AlN/$Al_{0.75}Ga_{0.25}N$ MQWs in accordance with the spectroscopic ellipsometry characterization. The additional potential modulation presented here is potentially useful for other material systems and functional devices to regulate quantum states with more degrees of freedom.

Author contributions

S. L., W. L., and J. K. conceived the idea, designed the experiments and wrote the manuscript. K. J., X. S., D. L., and J. L. contributed to the design of the MOVPE growth and discussion of the results. S. L., T. Z., H. C. and S. L. carried out characterization. Y. Z. and D. C. participated in the result discussion. The manuscript was written through contributions of all authors. All authors have given approval to the final version of the manuscript.

Conflicts of interest

The authors declare no competing financial interest.

Acknowledgements

W. He, S. Fang and T. Wu from Information and Network Center of Xiamen University are acknowledged for their help with the high performance computing. This work was supported by the National Natural Science Foundation of China (61874091, 61874090, 11804115, and 62135013) and the Key Scientific and Technological Program of Xiamen (3502ZCQ20191001, 3502Z20211002, and 3502Z20191016).

Notes and references

1 D. Li, K. Jiang, X. Sun and C. Guo, *Adv. Opt. Photonics*, 2018, **10**, 43.
2 L. Chen, J. Zheng, W. Lin, J. Li, K. Li, P. Sun, G. Guo and J. Kang, *ACS Photonics*, 2017, **4**, 2197–2202.
3 L. Chen, W. Lin, H. Wang, J. Li and J. Kang, *Light: Sci. Appl.*, 2020, **9**, 104.
4 Y. Taniyasu and M. Kasu, *Appl. Phys. Lett.*, 2011, **98**, 131910.
5 Y. Taniyasu, M. Kasu and T. Makimoto, *Appl. Phys. Lett.*, 2007, **90**, 261911.
6 R. G. Banal, M. Funato and Y. Kawakami, *Phys. Rev. B: Condens. Matter Mater. Phys.*, 2009, **79**, 121308.
7 T. M. Al Tahtamouni, J. Y. Lin and H. X. Jiang, *Appl. Phys. Lett.*, 2012, **101**, 042103.
8 K. B. Nam, J. Li, M. L. Nakarmi, J. Y. Lin and H. X. Jiang, *Appl. Phys. Lett.*, 2004, **84**, 5264–5266.
9 M. Leroux, N. Grandjean, M. Laügt, J. Massies, B. Gil, P. Lefebvre and P. Bigenwald, *Phys. Rev. B: Condens. Matter Mater. Phys.*, 1998, **58**, R13371–R13374.
10 T. Deguchi, K. Sekiguchi, A. Nakamura, T. Sota, R. Matsuo, S. Chichibu and S. Nakamura, *Jpn. J. Appl. Phys.*, 1999, **38**, L914–L916.
11 A. Aassve, N. Cavalli, L. Mencarini, S. Plach and M. Livi Bacci, *Science*, 2020, **369**, 370–371.
12 X. He, E. H. Y. Lau, P. Wu, X. Deng, J. Wang, X. Hao, Y. C. Lau, J. Y. Wong, Y. Guan, X. Tan, X. Mo, Y. Chen, B. Liao, W. Chen, F. Hu, Q. Zhang, M. Zhong, Y. Wu, L. Zhao, F. Zhang, B. J. Cowling, F. Li and G. M. Leung, *Nat. Med.*, 2020, **26**, 672–675.
13 H. Inagaki, A. Saito, H. Sugiyama, T. Okabayashi and S. Fujimoto, *Emerging Microbes Infect.*, 2020, 1744–1747.
14 X. Gonze, J.-M. Beuken, R. Caracas, F. Detraux, M. Fuchs, G.-M. Rignanese, L. Sindic, M. Verstraete, G. Zerah, F. Jollet, M. Torrent, A. Roy, M. Mikami, P. Ghosez, J.-Y. Raty and D. C. Allan, *Comput. Mater. Sci.*, 2002, **25**, 478–492.
15 M. D. Segall, P. J. D. Lindan, M. J. Probert, C. J. Pickard, P. J. Hasnip, S. J. Clark and M. C. Payne, *J. Phys.: Condens. Matter*, 2002, **14**, 2717–2744.
16 J. P. Perdew, K. Burke and M. Ernzerhof, *Phys. Rev. Lett.*, 1996, **77**, 3865–3868.
17 L. Qin, Y. Duan, H. Shi, L. Shi and G. Tang, *J. Phys.: Condens. Matter*, 2013, **25**, 045801.
18 R. Shinde, S. S. R. K. C. Yamijala and B. M. Wong, *J. Phys.: Condens. Matter*, 2021, **33**, 115501.
19 X. Jiang, J. Shi, M. Zhang, H. Zhong, P. Huang, Y. Ding, T. Yu, B. Shen, J. Lu and X. Wang, *New J. Phys.*, 2014, **16**, 113065.
20 Q. Yan, P. Rinke, A. Janotti, M. Scheffler and C. G. Van de Walle, *Phys. Rev. B: Condens. Matter Mater. Phys.*, 2014, **90**, 125118.
21 W. A. Harrison, *Elementary Electronic Structure*, World Scientific, 2004.
22 M. Peressi, N. Binggeli and A. Baldereschi, *J. Phys. D: Appl. Phys.*, 1998, **31**, 1273–1299.
23 D. Cai, J. Kang and G.-Y. Guo, *Phys. Rev. B: Condens. Matter Mater. Phys.*, 2009, **80**, 045311.
24 C. Tanguy, *Phys. Rev. Lett.*, 1995, **75**, 4090–4093.
25 W. Jiang, W. Lin, S. Li, J. Chen and J. Kang, *Opt. Mater.*, 2010, **32**, 891–895.
26 W. Lin, W. Jiang, N. Gao, D. Cai, S. Li and J. Kang, *Laser Photonics Rev.*, 2013, **7**, 572–579.
27 J. C. Slater and G. F. Koster, *Phys. Rev.*, 1954, **94**, 1498–1524.
28 Z. Zhu, Z. G. Fthenakis, J. Guan and D. Tománek, *Phys. Rev. Lett.*, 2014, **112**, 026803.
29 K. Jiang, X. Sun, Z. Shi, H. Zang, J. Ben, H.-X. Deng and D. Li, *Light: Sci. Appl.*, 2021, **10**, 69.
30 J. Li, W. Yang, S. Li, H. Chen, D. Liu and J. Kang, *Appl. Phys. Lett.*, 2009, **95**, 151113.
31 J. Li and J. Kang, *Phys. Rev. B: Condens. Matter Mater. Phys.*, 2005, **71**, 035216.
32 S.-H. Han, C.-Y. Cho, S.-J. Lee, T.-Y. Park, T.-H. Kim, S. H. Park, S. Won Kang, J. Won Kim, Y. C. Kim and S.-J. Park, *Appl. Phys. Lett.*, 2010, **96**, 051113.
33 Z. Chen, N. Fichtenbaum, D. Brown, S. Keller, U. K. Mishra, S. P. Denbaars and S. Nakamura, *J. Electron. Mater.*, 2008, **37**, 546–549.
34 A. M. Soomro, C. Wu, N. Lin, T. Zheng, H. Wang, H. Chen, J. Li, S. Li, D. Cai and J. Kang, *J. Phys. D: Appl. Phys.*, 2016, **49**, 115110.
35 E. Clementi, D. L. Raimondi and W. P. Reinhardt, *J. Chem. Phys.*, 1967, **47**, 1300–1307.
36 D. Y. Kim, J. H. Park, J. W. Lee, S. Hwang, S. J. Oh, J. Kim, C. Sone, E. F. Schubert and J. K. Kim, *Light: Sci. Appl.*, 2015, **4**, e263.
37 V. Y. Davydov, I. N. Goncharuk, A. N. Smirnov, A. E. Nikolaev, W. V. Lundin, A. S. Usikov, A. A. Klochikhin, J. Aderhold, J. Graul, O. Semchinova and H. Harima, *Phys. Rev. B: Condens. Matter Mater. Phys.*, 2002, **65**, 125203.
38 H. Harima, *J. Phys.: Condens. Matter*, 2002, **14**, R967–R993.
39 J. Zheng, J. Li, Z. Zhong, W. Lin, L. Chen, K. Li, X. Wang, C. Chou, S. Li and J. Kang, *RSC Adv.*, 2017, **7**, 55157–55162.

